

# Multiwavelength study of Cygnus A

## V. The hotspots in the lobe

S. Pyrzas<sup>1</sup>, K. C. Steenbrugge<sup>1,2</sup>, and K. M. Blundell<sup>2</sup>

<sup>1</sup> Instituto de Astronomía, Universidad Católica del Norte, Avenida Angamos 0610, Casilla 1280, Antofagasta, Chile  
e-mail: stylianos.pyrzas@gmail.com

<sup>2</sup> Department of Physics, University of Oxford, Keble Road, Oxford OX1 3RH, UK

Received 26 September 2014 / Accepted 28 November 2014

### ABSTRACT

**Context.** The jets in Fanaroff-Riley type II AGN are supposed to come to an abrupt halt in hotspots on opposite sides of the nucleus. Quite commonly, two hotspots are observed in each lobe. The origin of the second hotspot is currently poorly understood.

**Aims.** Our aims are to determine the origin of the secondary hotspot in the western lobe of Cygnus A from high resolution multifrequency radio images; to determine the minimum Lorentz factor of the electrons in the hotspots, often referred to as the low-energy turnover; and to study the magnetic field configuration of the hotspots.

**Methods.** We used 151 MHz Merlin and 327 MHz, 1.4, 5, 8, 15, and 43 GHz VLA images to determine the centroid of the peak luminosity, the spectral shape, and polarization fraction of both hotspots in the western lobe of Cygnus A.

**Results.** We find a spatial shift in peak luminosity between the lower and higher frequency images for both hotspots. We determine the minimum Lorentz factor of the electrons to be  $\sim 1000$ , and show that most of the emission from the primary hotspot is linearly polarized. The minimum energy magnetic field strength is found to range between  $\sim 0.14$  and  $\sim 0.5$  mG in both the primary and secondary hotspots.

**Conclusions.** From the low polarization and the determined outflow velocity, we conclude that the secondary hotspot is no longer a strong shock, and is an expanding, and hence a fading hotspot. This hotspot has an age that is of the same order of magnitude as the jet precession period.

**Key words.** galaxies: active – galaxies: individual: Cygnus A – galaxies: jets

## 1. Introduction

Cygnus A (3C 405) is a textbook example of a powerful Fanaroff-Riley type II (FR II) classical double radio galaxy. At a redshift of 0.056 07 (Owen et al. 1997), it is the closest of its kind and has therefore been studied extensively at radio wavelengths (e.g., Carilli et al. 1991).

In FR II radio galaxies the jets extending from the nucleus remain well collimated over several tens to hundreds of kpc and terminate in a shock, after running into the denser intergalactic medium. In the shock, the jet particles are reaccelerated and the electrons emit over a wide range of frequencies, from the radio to the X-ray bands. These shock regions are commonly referred to as hotspots.

Cygnus A displays a relatively common characteristic among radio galaxies, namely that two hotspots are detected per lobe, known to have different radio spectra, originally interpreted as being due to different ages. The primary hotspot in the western lobe, in this article denoted as LHS2, is smaller and is younger than the larger and more diffuse secondary hotspot, here denoted as LHS1 (Cox et al. 1991). The primary hotspot forms where the jet first encounters the intergalactic medium, or in the case of Cygnus A, the intracluster medium (ICM). The observed flux of the primary hotspot depends on the direction of the jet; in other words the primary hotspot at the end of the jet directed away from us will have a lower observed flux (Cox et al. 1991). This is indeed observed in Cygnus A (see, e.g., Table 1 in Steenbrugge et al. 2010).

The origin of the secondary hotspot is less certain, and the observed fluxes seem to be less or even not at all affected by

the jet direction. The secondary hotspot is generally farther from the nucleus (Williams & Gull 1985), as is also observed in Cygnus A. The secondary hotspot could be formed by jet plasma leaving the primary hotspot, which is then an oblique shock, at an angle such that the jet plasma stays supersonic. The jet impacting the ICM at an angle can be attributed to precession of the jet, or to the interaction between the jet and backflowing plasma. In the latter case the secondary hotspot is called a splatter spot (Williams & Gull 1985). Alternatively, in the dentist's drill model (Scheuer 1982), the secondary hotspot formed at the previous impact point of the jet, and the jet has since changed direction, possibly because of precession. In this model, particles can still enter the secondary hotspot, but this plasma is no longer supersonic. The difference between these models is thus whether or not the secondary hotspot is replenished with supersonic plasma.

Cygnus A is an ideal target with which to test the different theories of the formation of secondary hotspots because of its relative closeness and the extensive high quality radio data available. From previous work, we know that the jets are precessing and that the jet speed is less than  $0.5c$ , a relatively low value (Steenbrugge et al. 2010). We also know that Cygnus A is moving through the cluster, with a radial velocity offset of at least  $163 \text{ km s}^{-1}$  (Ledlow et al. 2005) and a similar order of magnitude proper motion (Steenbrugge et al. 2014). Hence, the direction of the jet certainly changes over time in this source.

In Steenbrugge et al. (2008) we determined a minimum Lorentz factor of  $\lesssim 10^3$  in the jets from the combination of (i) the X-ray luminosity due to the inverse-Compton scattering of the cosmic microwave background photons (ICMB) by electrons



**Fig. 1.** Main panel: Cygnus A at 15 GHz. North is up, east to the left. *Inset panels:* A detailed view of the lobe (*right*) and counterlobe (*left*) regions, showing the four hotspots detected in Cygnus A.

present in a relic jet; (ii) the upper limit to the X-ray ICCMB luminosity of the current jets; and (iii) the lack of radio emission from the relic jet. Studying the hotspots gives us an opportunity to determine the minimum Lorentz factor of the electrons in an independent manner, as was done by Carilli et al. (1991) for lower resolution radio data.

Throughout this paper we will use the term lobe to refer to the lobe closest to Earth (i.e., on the western, approaching side) and counterlobe to refer to its more distant counterpart (i.e., on the eastern, receding side). Similarly, we denote the lobe hotspots as LHS 1&2 and the counterlobe hotspots as CHS 1&2. In Fig. 1, we show an image of Cygnus A at 15 GHz with a close-up view of the lobe and counterlobe denoting the four hotspots.

Here, we focus our analysis solely on the lobe and defer the analogous analysis of the counterlobe to a future paper. To our knowledge, this is the first time such an analysis is performed for the primary hotspot, LHS2, as most of the available literature focuses on the secondary hotspot, LHS1. The structure of the paper is as follows: in Sect. 2 we briefly present the data used and their reduction. Our analysis is detailed in Sect. 3, while in Sect. 4 we present the results from our analysis. In Sect. 5 we discuss our results, and finally we summarize our findings in Sect. 6.

## 2. Observations and reductions

In our analysis we used seven archival radio data sets, obtained with the Multi-Element Radio-Linked Interferometer Network (MERLIN<sup>1</sup>) and the Very Large Array (VLA<sup>2</sup>). All data sets have been previously published and were reduced by the respective authors; we undertook no further processing of the data. An overview of these data is given in Table 1.

MERLIN observations of Cygnus A were conducted at 151 MHz, the lowest frequency used in this paper. The data were kindly provided by Paddy Leahy and were first published in Leahy et al. (1989). VLA observations were obtained at 327 MHz, 1345 MHz, 5 GHz, 8 GHz, 15 GHz and 43 GHz. At all frequencies, data from the different VLA configurations were

**Table 1.** Overview of data sets used.

Tel.	Freq. [MHz]	Config.	Pixel scale ["/pix.]	Beam size [arcsec <sup>2</sup> ]
MERLIN	151		0.5	3.00 × 3.00
VLA	327	A	0.5	2.50 × 2.50
	1345	ABCD	0.3	1.40 × 1.32
	4525	ABCD	0.125	0.40 × 0.40
	8515	ABCD	0.05	0.25 × 0.21
	14655	ABCD	0.125	0.35 × 0.35
	43340	ABC	0.013	0.07 × 0.06

combined. The data were kindly supplied by Chris Carilli and were first published in Carilli et al. (1991, 1996, 1999), Carilli & Barthel (1996) and Perley & Carilli (1996).

The data span a wide range in cell sizes, from 0.5"/pixel for the 151 and 327 MHz images to 0.013"/pixel for the 43 GHz image. More details about the radio data can be found in Steenbrugge et al. (2010) and Steenbrugge & Blundell (2008). For all frequencies, except 43 GHz, both lobes and the nucleus are registered on one image. At 43 GHz however, three different images were obtained, one for the nucleus, and one for the outer part of each lobe.

We also made use of *Chandra* X-ray data in our analysis. We used eight different observations obtained with the ACIS-I camera in VFaint mode. After calibration, using CIAO 3.3 and CALDB 3.2.2, and alignment of the individual images, we combined the eight different images to create the total image used in this analysis. The energy range in this resultant data set is between 0.2 and 10 keV. Further details on the data reduction, alignment and stacking of the eight different observations are given in Steenbrugge et al. (2008).

## 3. Analysis

### 3.1. Hotspot morphology

The high spatial resolution of the 43 GHz data offers us a chance to study the hotspot morphology in detail. In Figs. 2 and 3 we show a close-up view of both hotspots in the western lobe at 43 GHz.

<sup>1</sup> MERLIN is a National Facility operated by the University of Manchester at Jodrell Bank Observatory on behalf of PPARC/STFC.

<sup>2</sup> The VLA is a facility of the National Radio Astronomy Observatory, National Science Foundation.

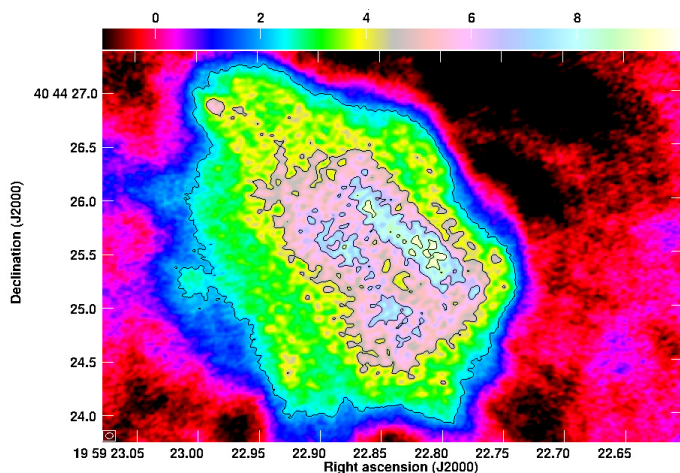


**Fig. 2.** Close-up view of LHS1 at 43 GHz. A linear feature is clearly visible, as well as indication of additional substructure.

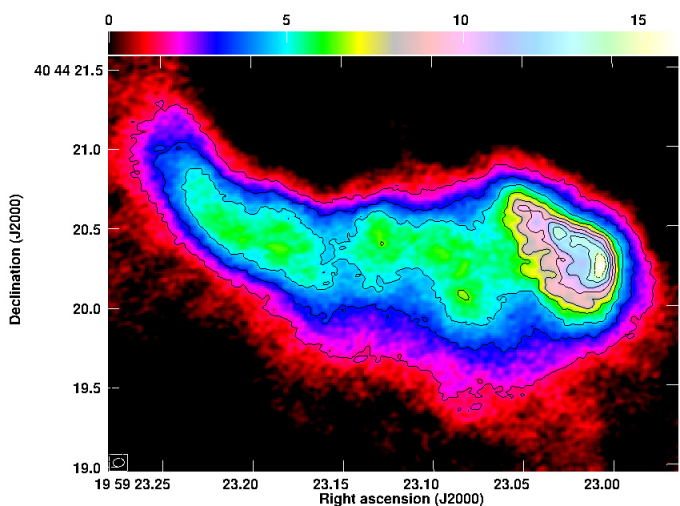


**Fig. 3.** Close-up view of LHS2 at 43 GHz. We note the elongated area of strongest emission in the nucleus.

LHS1 (Fig. 2) is roughly rectangular in shape with an approximate size of  $1.3'' \times 2.0''$ , embedded in an elongated cloud of diffuse emission. The western edge of this cloud also marks the edge of the lobe itself. Easily visible is a linear structure of increased emission, towards the edge of the lobe, that could represent the terminal-jet shock (Carilli et al. 1999). There is also evidence of additional substructure in this hotspot, in the form of two discrete “bubbles” of emission that could be part of a second, though dispersed, linear structure (see also Fig. 5).

LHS2 differs significantly in shape and shows a tadpole-like nucleus, about  $0.7'' \times 1.2''$  in size, with an eastward extending tail of diffuse emission that also bends northwards (see Fig. 3). Interestingly, the area of strongest emission in the nucleus of LHS2 appears also to be elongated, perhaps an indication towards a barely resolved linear structure, similar to that seen in LHS1.

### 3.2. Hotspot photometry

The analysis presented in this paper is built around the determination of the flux densities of the hotspots.

An immediate obstacle in this calculation is defining the actual, spatial extent of the hotspots; in other words determining

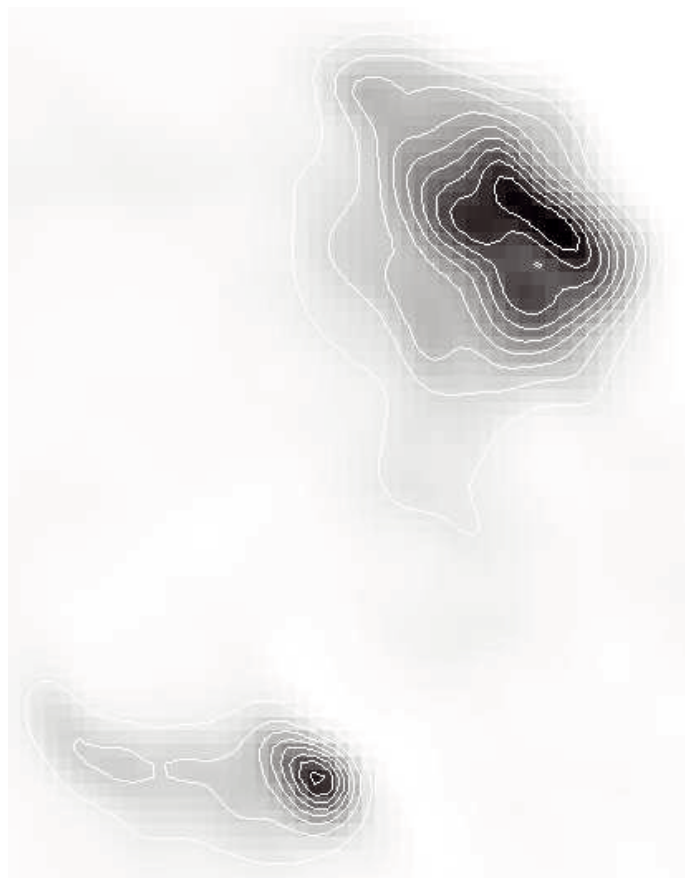


**Fig. 4.** Detail of the 15 GHz image showing both hotspots, with the 8 GHz data overlaid as contours.

where the hotspots end and the lobe begins. We did the following to tackle this problem: we selected the 8 GHz data as our reference data. This was done because the 8 GHz data have a high spatial resolution, second only to the 43 GHz data; but also the entire (radio)galaxy, i.e., both lobes and the nucleus, is contained in a single image, in contrast to the 43 GHz data.

Both hotspots as observed at 15 GHz, with the 8 GHz contours overplotted, are shown in Fig. 4. The hotspots as observed at 8 and 15 GHz have the same morphology and position. The morphology is also consistent with that observed at 43 GHz. Because of the lower resolution at lower frequencies, it is not possible to compare the morphology of the hotspots over a larger frequency range.

Subsequently, we defined two reference photometry apertures, one for each hotspot in the lobe. The aperture definition was done by eye, according to what we considered to be the extent of LHS 1 & 2; this step is unavoidably subjective. Furthermore, for LHS2, the primary hotspot, the lack of resolution in all but the 43 GHz image, made us compromise and choose a larger area which could be studied in all bands. The apertures themselves are shown in Fig. 5, while we provide additional information on the definition of the apertures in Table 2. We note that for defining the apertures, all images were rotated clockwise by 38 degrees, to align LHS1 in the XY-direction. We then applied these apertures, based solely on their coordinates, on all available data. This ensured consistency in our measurements.

A second obstacle for determining the hotspot flux densities arises because the hotspots are embedded in a background of diffuse lobe plasma emission, which introduces an uncertainty in

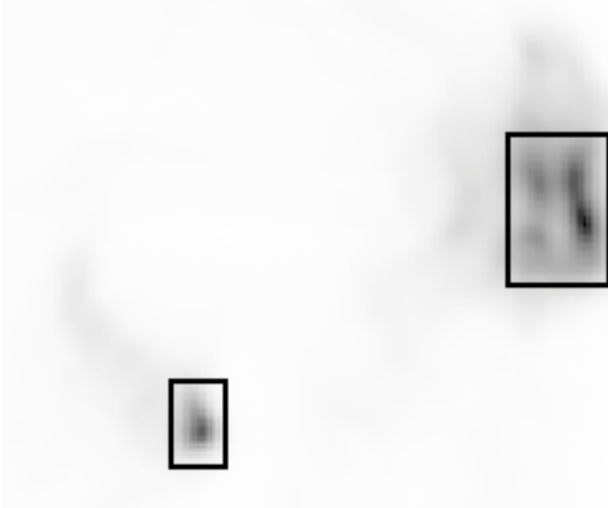


**Fig. 5.** Detail of the outer part of the lobe of Cygnus A at 8 GHz. The image has been rotated clockwise by an angle of 38 degrees in order to achieve alignment of the linear feature in LHS1 with the  $y$ -axis. The reference photometry apertures around LHS1 and LHS2 are shown.

**Table 2.** Details on the two reference apertures used in our photometry.

Spot	BLC		TRC	
	RA 19:59:xx.xxx	Dec +40:44:xx.xxx	RA 19:59:xx.xxx	Dec +40:44:xx.xxx
LHS1	22.840	24.253	22.856	26.590
LHS2	23.018	19.693	23.033	20.960

**Notes.** Both apertures were rectangular, and for each aperture we provide RA and Dec coordinates of the bottom-left (BLC) and top-right (TRC) corners, respectively. To define the apertures, the 8 GHz image was rotated clockwise by an angle of 38 degrees.

the flux determination. As this emission is highly non-uniform, it is difficult to account for it. A final difficulty in distinguishing between actual hotspot and lobe background flux comes from the wide range of resolutions in our data set, particularly in the MHz bands, where the hotspots are not resolved. In an attempt to quantify and correct this background emission<sup>3</sup>, we also defined 16 background apertures, eight for each hotspot. These apertures had exactly the same size as the photometry aperture and surrounded it completely on all sides, creating a  $3 \times 3$  pattern with the photometry aperture at the center.

### 3.3. A shift of maximum emission positions

While applying the coordinate-based apertures on each image, it quickly became apparent that the apertures did not match the observed hotspot profiles in the lower frequency images, i.e., 151 MHz, 327 MHz and 1.5 GHz, although they accurately described the profiles at 5 GHz, 15 GHz and 43 GHz. This inconsistency is visualized in Fig. 6 and we decided that this shift was worth further scrutiny.

As a first step, we measured the positions (RA and Declination) of the maximum observed emission for the hotspots in all bands using a combination of AIPS/IMCENTER and MAXFIT. With the 8 GHz image still acting as reference, we then calculated the shift between these positions. These shifts are

<sup>3</sup> The actual sky background is negligible, because these are interferometric images.

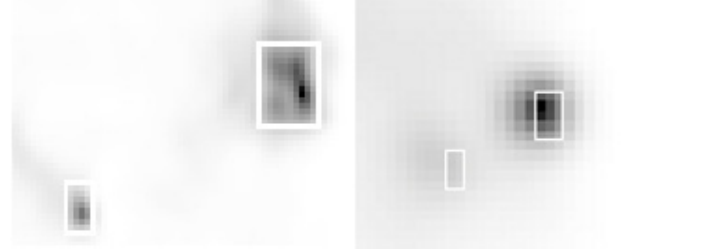


**Fig. 6.** Apparent shift of the hotspot positions between the radio bands. *Left:* the 15 GHz image with the reference photometry apertures superimposed. Both apertures fit the hotspot profiles well. *Right:* the same, but for the 327 MHz image. The shift between hotspot and aperture position is evident, particularly for LHS2.

reported in Table 3. A quick inspection reveals, at least at face value, shifts of about half an arcsecond or more in the lowest frequency bands. In addition, the shifts in these bands are consistently  $\Delta\text{RA} < 0$  and  $\Delta\text{Dec} > 0$  indicating a SE shift, i.e., towards the direction of the nucleus.

One potential culprit for these shifts could be erroneous astrometric calibration. We thus checked the position of the nucleus in our data, repeating the process employed above for the hotspots. The measured shifts, with the unfortunate exception of the MHz bands in which the nucleus is not detected, are also reported in Table 3. It is evident that the discrepancy in maximum emission position cannot be attributed to the astrometric calibration.

Another potential culprit could be the reduced resolution of the lower frequency images. To account for this effect, we convolved and rebinned the 8 GHz image to match the resolution and pixel size of the 151 MHz, 327 MHz and 1.5 GHz data and repeated the measurements on the new images, i.e., calculated the shift in position with respect to the original 8 GHz image. These shifts are also reported in Table 3 and indicate that the reduced resolution can indeed introduce significant shifts in the maximum emission position. We also note that, wherever present, the difference in position between the original and the convolved images is always  $0.5''$ , which is the pixel scale of the MHz data. However, there is still an offset between the centroid of the low frequency and deconvolved 8 GHz peak luminosity for both hotspots. The offset is largest for the primary hotspot, LHS2, which can be seen in Fig. 7. In this figure we show the 327 MHz data and overplot the convolved 8 GHz  $\rightarrow$  327 MHz image as contours. The two panels differ only by a change in grayscale used, the left one is optimized to compare LHS1, while the right one is optimized to compare LHS2.

Although an analysis of the counterlobe is not the subject of this paper, we repeated the process described above for the counterlobe hotspots, to check whether a shift in hotspot emission is detected there too. The last two columns of Table 3 report the measured shifts. The shifts in this case have  $\Delta\text{RA} > 0$  and  $\Delta\text{Dec} < 0$ , indicating a NW shift, i.e., again towards the direction of the nucleus.

A shift between the radio and X-ray peak emission of hotspots has been seen in several radio galaxies, (see, e.g., Blundell et al. 2006; Perlman et al. 2010; Erlund et al. 2010; Blundell & Fabian 2011). Considering that we detect a shift between the low-frequency and the high-frequency radio emission from the hotspots, we also overlaid the X-ray data to determine whether a similar shift is detected. In Figs. 8 and 9 we show this overlay using the 15 GHz radio image. The difference between both images is the grayscale used, the former is optimized to

**Table 3.** Calculated RA and Dec shifts in the hotspot maximum emission position for all bands.

Frequency	Ref. position of LHS1 @ 8 GHz		Ref. position of LHS2 @ 8 GHz		Ref. position of the core @ 8 GHz		Ref. position of CHS1 @ 8 GHz		Ref. position of CHS2 @ 8 GHz	
	$\Delta$ RA	$\Delta$ Dec	$\Delta$ RA	$\Delta$ Dec	$\Delta$ RA	$\Delta$ Dec	$\Delta$ RA	$\Delta$ Dec	$\Delta$ RA	$\Delta$ Dec
43 GHz	+115.9	-25.7	+88.6	+29.2	$_{-}^a$	$_{-}^a$	$_{-}^a$	$_{-}^a$	$_{-}^a$	$_{-}^a$
15 GHz	-51.1	-14.7	-80.7	-27.3	+17.0	+110.8	+120.5	-11.6	+73.9	+38.5
5 GHz	-45.5	-32.8	-75.0	-45.4	+22.7	-32.5	+126.2	-30.0	+79.6	+20.1
1.5 GHz	-451.2	+167.0	-328.5	+5.9	-31.8	+120.2	+347.8	+24.2	+2.3	-202.3
CONV: 8 GHz $\rightarrow$ 1.5 GHz	-451.2	+167.6	-328.5	+5.9	-	-	-	-	-	-
327 MHz	-987.6	+341.4	-1237.7	+91.3	$_{-}^b$	$_{-}^b$	+61.4	-261.3	$_{-}^c$	$_{-}^c$
CONV: 8 GHz $\rightarrow$ 327 MHz	-487.6	+341.5	-737.6	+91.4	-	-	-	-	-	-
151 MHz	-355.7	+710.9	-605.8	+461.0	$_{-}^b$	$_{-}^b$	+1131.0	-354.9	$_{-}^c$	$_{-}^c$
CONV: 8 GHz $\rightarrow$ 151 MHz	-855.8	+210.8	-605.8	-39.0	-	-	-	-	-	-
X-Ray	-436.4	+6.8	-151.2	-322.6	-	-	-	-	-	-

**Notes.** The reference positions at 8 GHz are RA = 19:59:22.8166, Dec = 40:44:25.5268 for LHS1 and RA=19:59:23.0147, Dec = 40:44:20.2774 for LHS2. The fourth column gives the shifts in the maximum emission position of the nucleus across the bands, when the nucleus is detected. The last two columns list the shifts between the hotspots in the counterlobe, if detected. All shifts are given in milli-arcseconds. <sup>(a)</sup> Three different images were obtained at 43 GHz to sample the hotspots in the lobe and counterlobe and to detect the nucleus. <sup>(b)</sup> The core is not detected at the MHz bands. <sup>(c)</sup> CHS2 is not detected at the MHz bands.

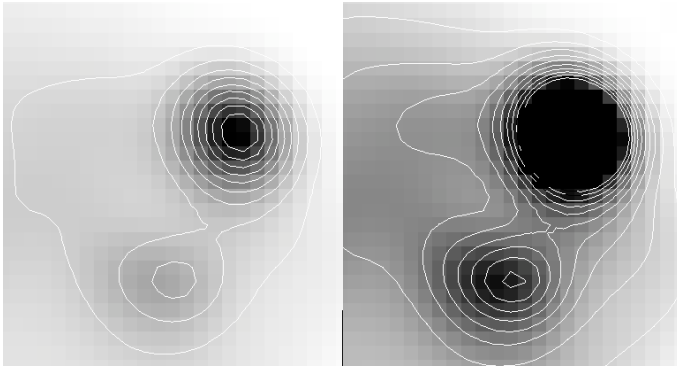


**Fig. 7.** 327 MHz data (grayscale) and the convolved 8 GHz  $\rightarrow$  327 MHz (contours). The two panels differ in the choice of grayscale and contour levels, to highlight LHS1 (left panel) and LHS2 (right panel). We note the mismatch between grayscale and contours in LHS2.

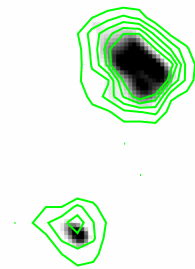


**Fig. 8.** 15 GHz image of the hotspots in the lobe with the *Chandra* 0.2–10 keV contours overlaid. The contour levels are logarithmically spaced and between 20 and 70 counts. The grayscale is optimized to see any potential shift in emission for the secondary hotspot.

detect any possible shift in the secondary hotspot, LHS1, while the latter is optimized for studying LHS2.

Figures 8 and 9 indicate that there is indeed a shift in the X-ray emission compared to the radio emission for the primary hotspot; however, no shift in emission is seen for the secondary hotspot. In contrast to other cases where a shift between radio and X-ray emission is observed, the X-ray and radio emission from the hotspots of Cygnus A are partially co-spatial. The

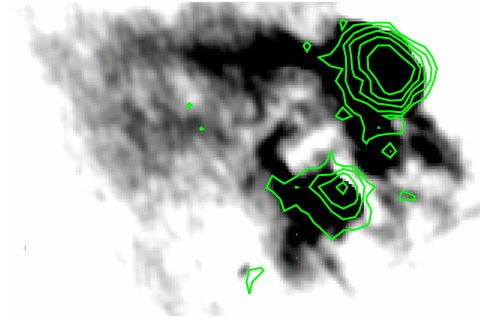


**Fig. 9.** Same as Fig. 8 but now optimized for studying LHS2. The contours are logarithmically spaced between 13 and 70 counts. We note the weak radio and completely offset X-ray emission, which might be a jet knot or a very young hotspot.

X-ray emission of the primary hotspot is shifted to a larger distance from the nucleus, extending the shift observed between the low and high frequency images.

In Fig. 9, a weak emission feature is visible to the SE of LHS2, that could be explained as a third hotspot or a jetknot. In this case, the radio and X-ray emission are completely offset, with the offset following the direction of the shift observed in the primary hotspot. However, the radio and X-ray emission of this feature are too weak for further study of these images. We note that this feature is not detected at lower frequencies.

## 4. Results

### 4.1. Hotspot flux densities

Using our reference photometric apertures we measured the flux density of LHS1 and LSH2 using standard techniques with AIPS/IMSTAT. Our measurements are summarized in Table 4.

To account for the diffuse lobe emission we used the eight background apertures around each hotspot, detailed in Sect. 3.2. As background flux, we set the highest measured value among all eight apertures. These measurements are reported in Table 4. We note that these values consistently corresponded to the same background aperture on all bands.

**Table 4.** Flux density measurements (flux) and background measurements (bckg) for both hotspots in the lobe of Cygnus A in all seven bands.

Spot	Flux density [Jy]									
	151 MHz	327 MHz	1345 MHz	5 GHz	8 GHz	15 GHz	43 GHz	15 GHz POL	43 GHz POL	
LHS1 <sub>flux</sub>	71.71	47.99	46.07	21.08	11.60	8.21	3.45	1.60	1.66	
LHS1 <sub>bckg</sub>	59.25	42.15	19.93	7.87	4.04	2.59	1.42	0.71	0.78	
shLHS1 <sub>flux</sub> *	72.55	51.72	46.52	–	–	–	–	–	–	
shLHS1 <sub>bckg</sub> *	52.03	33.88	15.24	–	–	–	–	–	–	
LHS2 <sub>flux</sub>	21.37	10.67	4.86	3.59	2.16	1.59	0.82	0.46	0.49	
LHS2 <sub>bckg</sub>	22.07	12.28	4.80	1.78	0.86	0.67	0.46	0.06	0.12	
shLHS2 <sub>flux</sub> *	22.17	12.73	5.31	–	–	–	–	–	–	
shLHS2 <sub>bckg</sub> *	20.79	11.58	3.88	–	–	–	–	–	–	

**Notes.** The last two columns give the flux density and background measurements of the 15 GHz and 43 GHz polarization data. Also listed are the flux and background measurements in the lower frequency bands, after repositioning the photometric aperture to account for the shift in hotspot position detailed in Sect. 3.3. (\*) Shifted aperture position. See Sect. 3.3 for details.

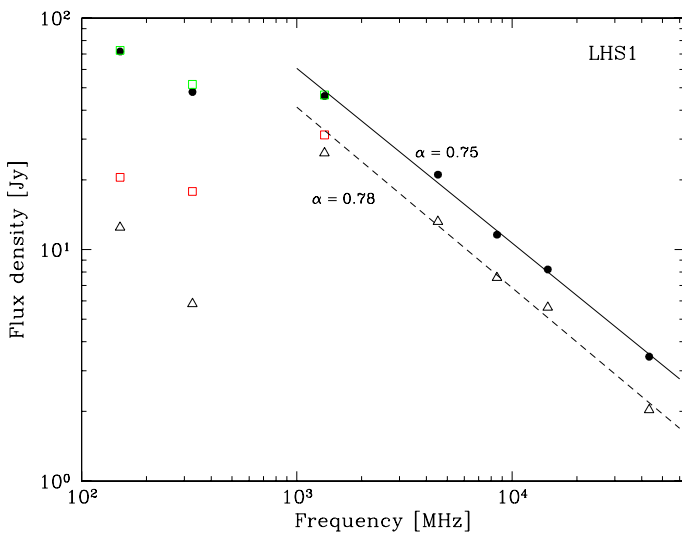


**Fig. 10.** Flux density measurements for LHS1. Filled circles correspond to the original flux measurements, open triangles to the background corrected ones. Green open squares are measurements after repositioning the reference photometry aperture, while red open squares are the corresponding background corrected values. The straight line is a linear fit to the original flux measurements, the dashed line is a linear fit to the background corrected ones.

For the low frequency data we also had to reposition our reference aperture to account for the shift, as described in the previous Section, and repeat the measurements. Table 4 lists both the original values and the ones obtained after repositioning the aperture.

A graphic representation of Table 4 is given in Figs. 10 and 11. The lobe spectra of Cygnus A, similar to many radio galaxies, show low-frequency curvature (Rudnick et al. 1994; Duffy & Blundell 2012). However, the resolution at low frequencies, the limited number of frequencies used, and the large lobe component prevents us from testing whether the hotspot spectra themselves are curved at low frequencies. We performed two linear fits for each hotspot, one using the straightforward flux values (fl) and one using the background corrected flux values (bc). Given the reduced resolution and the uncertainty in hotspot position we restricted the fit only to the GHz bands for LHS1 and to the GHz bands excluding 1.5 GHz for LHS2, as LHS2 is more heavily affected by resolution because of its smaller size.

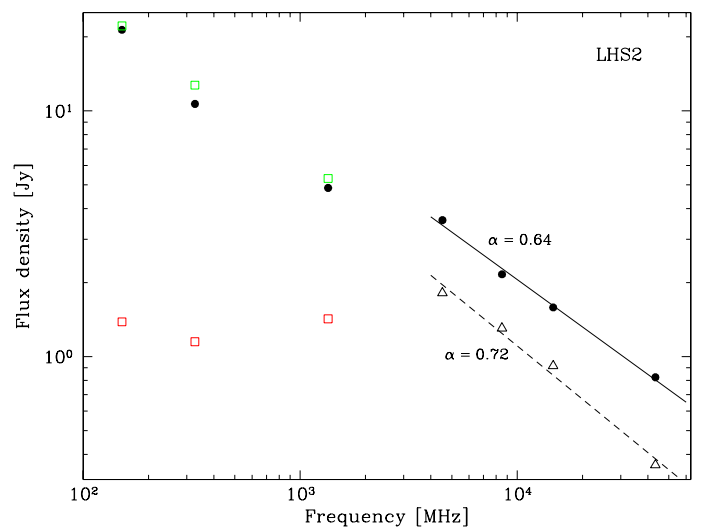


**Fig. 11.** Same as Fig. 10 but for LHS2. We note that the background corrected values (open triangles) for the original flux measurements of the lower frequency data are missing, as they are negative (see Table 4).

For the spectral index<sup>4</sup> for LHS1 we use the fluxes between 1.4 and 43 GHz to obtain  $\alpha_{\text{fl}}^{\text{LHS1}} = 0.75 \pm 0.02$  and  $\alpha_{\text{bc}}^{\text{LHS1}} = 0.78 \pm 0.03$  for the original and background corrected fluxes, respectively. For LHS2, the fluxes between 5 and 43 GHz were used and the corresponding values are  $\alpha_{\text{fl}}^{\text{LHS2}} = 0.64 \pm 0.03$  and  $\alpha_{\text{bc}}^{\text{LHS2}} = 0.72 \pm 0.06$ .

#### 4.2. Polarization

We used the 15 and 43 GHz polarization data to study the degree of polarization (DOP) of the lobe and hotspot emission. The photometry on the polarization data was performed in the exact same manner, i.e., using our reference apertures. The values are reported in Table 4.

In Figs. 12 and 13 we show the total intensity (Stokes  $I$ ) and the polarized (Stokes  $Q$  and  $U$ ) 43 GHz emission for both hotspots. Comparing the two figures, we see that the linear structure observed in  $I$  for LHS1 disappears in  $Q$  and  $U$ . For LHS2 on the other hand a clear structure is seen in both the total intensity and the polarized image. The bright rim observed in LHS2 is highly polarized, and easily identified.

<sup>4</sup> We adopt a power-law of the form  $L_{\nu} \propto \nu^{-\alpha}$ .

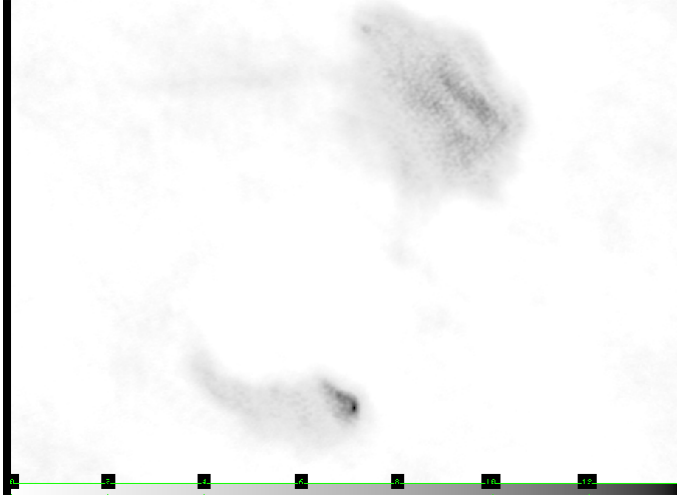


**Fig. 12.** The 43 GHz flux observed in Stokes  $I$ , detailing the two hotspots in the lobe. In LHS1 two linear substructures, which could be linear shockfronts, can be observed. In LHS2 a bright point is visible with a weaker linear structure above it, extending to the NE.

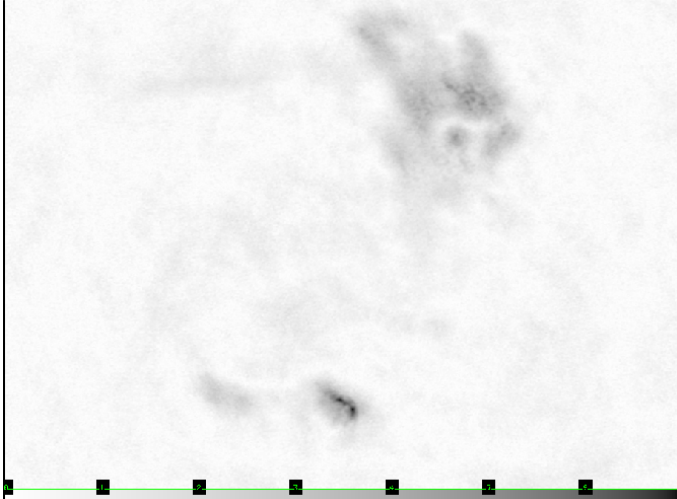


**Fig. 13.** Same as Fig. 12, but for the combined Stokes  $Q$  and  $U$ , and thus detailing the polarized emission. The linear substructures as observed in  $I$  band for LHS1 have disappeared. Instead a rather chaotic structure is visible. For LHS2 we observe again the bright point; the NE extending linear feature is more prominent.

A straightforward division between the flux densities of the total intensity and polarized 15 GHz data yields  $DOP_{\text{fl}}^{\text{LHS1}} = 19.48\%$  and  $DOP_{\text{fl}}^{\text{LHS2}} = 28.77\%$  for LHS1 and LHS2, respectively. Using the background corrected flux densities for the same calculation yields  $DOP_{\text{bc}}^{\text{LHS1}} = 15.77\%$  and  $DOP_{\text{bc}}^{\text{LHS2}} = 43.18\%$ . The low degree of polarization for LHS1 is also seen in Fig. 14, which shows that the immediate surroundings of LHS1 are more highly polarized than the spot region itself, while the opposite is true for LHS2. Redoing the calculation for the 43 GHz data, we find  $DOP_{\text{fl}}^{\text{LHS1}} = 48.23\%$  and  $DOP_{\text{fl}}^{\text{LHS2}} = 58.86\%$ . Using the background corrected fluxes we calculate a  $DOP_{\text{bc}}^{\text{LHS1}} = 43.62\%$  and  $DOP_{\text{bc}}^{\text{LHS2}} = 100\%$ . A DOP of 100% is unrealistic, and is due to the large fraction of background in the image for this much weaker hotspot. We note that for background correction we subtracted the largest measured flux as determined from the eight different background apertures.

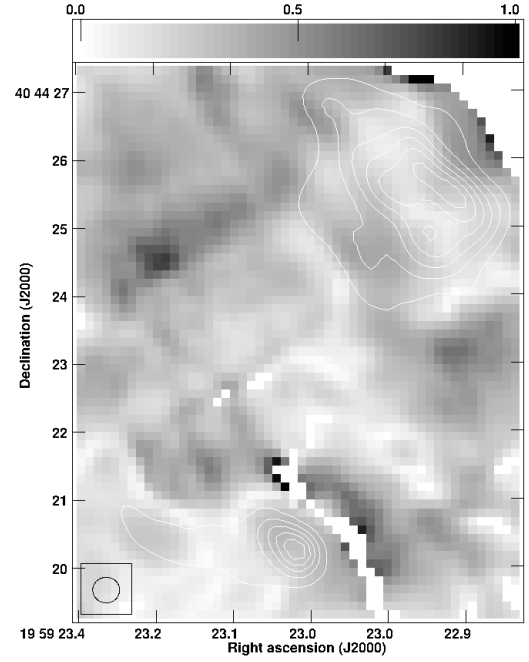


**Fig. 14.** Fractional polarization image of the lobe at 15 GHz. We overplot the 15 GHz data as contours, to aid the eye in the identification of the hotspots position. Certain pixels were blanked and appear white; for these pixels the polarized flux value was nominally larger than the unpolarized value, most likely a data artifact.

The fractional polarization is twice as large for 43 GHz than for 15 GHz, with most of the emission from LHS2 detected at 43 GHz being linearly polarized emission. We also note that the polarized flux increases between 15 and 43 GHz for both hotspots, while the total flux decreases.

Using the 15 GHz image, we created a fractional polarization image to get a clearer view of the DOP; this is shown in Fig. 14.

#### 4.3. Minimum magnetic field

To calculate the magnetic field strength in the hotspots we assume that the spectrum of the radiation is a power-law of the form  $L_{\nu} \propto \nu^{-\alpha}$  and that the emission mechanism is synchrotron radiation. Then, for a volume  $V$  which at a certain frequency  $\nu$  has a given luminosity  $L_{\nu}$ , the electron energy spectrum is

$$N(E)dE = E_0 E^{-(2\alpha+1)}dE \quad (1)$$

or equivalently

$$N(\gamma)d\gamma = N_0 \gamma^{-(2\alpha+1)}d\gamma \quad (2)$$

with  $N_0 = E_0/(m_e c^2)^{2\alpha}$ . The radio luminosity is related to the energy spectrum of the relativistic electrons and the magnetic field  $B$  by

$$L_{\nu} = A V N_0 B^{1+\alpha} \nu^{-\alpha}, \quad (3)$$

where the first term  $A$  is effectively a constant given by

$$A = 2.344 \times 10^{-25} \left(1.253 \times 10^{37}\right)^{\alpha} a(2\alpha + 1)(m_e c^2)^{2\alpha} \quad (4)$$

with values for  $a(2\alpha + 1)$  given in Table 18.2 of Longair (1994). The total energy present in the given volume, responsible for the emission, is a combination of the energy in electrons (we assume

**Table 5.** Calculated values of the minimum energy magnetic field  $B_{\min}$  based on our flux density measurements for the high frequency data.

$\gamma$	5 GHz				8 GHz				15 GHz				43 GHz			
	flux	cflux	flux	cflux												
$B_{\min}$ LHS1 [mG]																
	$\alpha = 1$	$\alpha = 0.75$	$\alpha = 0.78$		$\alpha = 1$	$\alpha = 0.75$	$\alpha = 0.78$		$\alpha = 1$	$\alpha = 0.75$	$\alpha = 0.78$		$\alpha = 1$	$\alpha = 0.75$	$\alpha = 0.78$	
$10^0$	1.21	1.08	0.55	0.53	1.26	1.13	0.55	0.54	1.29	1.17	0.54	0.54	1.42	1.25	0.56	0.54
$10^1$	0.68	0.61	0.40	0.38	0.71	0.63	0.40	0.38	0.72	0.66	0.40	0.39	0.80	0.70	0.41	0.39
$10^2$	0.38	0.34	0.30	0.27	0.40	0.36	0.30	0.27	0.41	0.37	0.29	0.27	0.45	0.39	0.30	0.28
$10^3$	0.22	0.19	0.22	0.19	0.22	0.20	0.22	0.19	0.23	0.21	0.22	0.20	0.25	0.22	0.22	0.20
$10^4$	0.12	0.11	0.16	0.14	0.13	0.11	0.16	0.14	0.13	0.18	0.16	0.14	0.14	0.13	0.16	0.14
$B_{\min}$ LHS2 [mG]																
	$\alpha = 1$	$\alpha = 0.64$	$\alpha = 0.72$		$\alpha = 1$	$\alpha = 0.64$	$\alpha = 0.72$		$\alpha = 1$	$\alpha = 0.64$	$\alpha = 0.72$		$\alpha = 1$	$\alpha = 0.64$	$\alpha = 0.72$	
$10^0$	1.21	1.02	0.39	0.41	1.32	1.16	0.41	0.45	1.32	1.15	0.39	0.43	1.62	1.32	0.44	0.46
$10^1$	0.68	0.57	0.33	0.31	0.74	0.65	0.34	0.35	0.74	0.65	0.32	0.33	0.91	0.74	0.37	0.35
$10^2$	0.38	0.32	0.28	0.24	0.42	0.37	0.29	0.26	0.42	0.36	0.27	0.25	0.51	0.42	0.31	0.27
$10^3$	0.21	0.18	0.23	0.18	0.23	0.21	0.24	0.20	0.23	0.20	0.23	0.19	0.29	0.24	0.26	0.20
$10^4$	0.12	0.10	0.19	0.14	0.13	0.12	0.20	0.15	0.13	0.12	0.19	0.15	0.16	0.13	0.22	0.16

**Notes.** We have calculated  $B_{\min}$  both for the straightforward flux measurement (flux) and for the background subtracted value (cflux). We have also repeated our calculation for a general spectral index of  $\alpha = 1$ , as well as for the spectral indices calculated from fitting our photometry (see Figs. 10 and 11). In all cases, we have performed the calculation for five different  $\gamma$  values.

that proton contribution,  $K$ , is negligible) and the energy in the magnetic field, and is given by the equation

$$E_{\text{tot}} = \frac{Vm_e c^2}{2\alpha - 1} \frac{L_\nu}{AVB^{1+\alpha}\gamma^{-\alpha}} \frac{1}{\gamma_{\min}^{2\alpha-1}} + V \frac{B^2}{2\mu_0} + K, \quad (5)$$

where we used Eq. (3) to substitute for  $N_0$  and  $\gamma_{\min}$  is the minimum Lorentz factor of the electrons. Under minimum energy conditions, we can differentiate Eq. (5) with respect to  $B$ , equate the derivative with zero and solve for  $B$ . This yields

$$B_{\min} = \left[ \frac{\mu_0}{V} \frac{1}{\gamma_{\min}^{2\alpha-1}} (1 + \alpha) \frac{m_e c^2}{2\alpha - 1} \frac{L_\nu}{AV^{-\alpha}} \right]^{\frac{1}{3+\alpha}}. \quad (6)$$

This is the magnetic field strength determined assuming minimum energy conditions, and we will call it the minimum energy magnetic field.

The biggest hurdle in calculating the minimum energy magnetic field is the source volume  $V$  which is generally not known. In what follows we assume a cylindrical volume of the form  $V = \pi r^2 \ell$ , where  $\ell$  corresponds to the long side and  $r$  to half the short side of our rectangular photometric apertures describing each hotspot.

We assume a geometry with  $\Omega_\Lambda = 0.7$ ,  $\Omega_M = 0.3$  and  $H_0 = 73 \text{ km s}^{-1} \text{ Mpc}^{-1}$ . At a redshift  $z = 0.05607$  this corresponds to a distance  $d = 227.3 \text{ Mpc}$  and a scale size of  $1.044 \text{ kpc}''$ .

Under these assumptions we have calculated the minimum energy magnetic field strength using our flux density measurements (Table 4) and Eq. (6), for different values of  $\gamma_{\min}$ . The results are reported in Table 5 and shown in Fig. 15. We have restricted our calculations to the high frequency data, i.e., 5 GHz and above, for the following two reasons. First, because of the previously discussed shift in peak emission at low frequency data, and second because of the lower resolution of these data. This impedes the deblending of the hotspot emission from the lobe emission, with the latter also being brighter at low frequencies, compared to the high frequencies.

Table 5 shows  $B_{\min}$  values ranging from a little over a milli Gauss (mG) to a tenth of a mG in both hotspots, depending on the different combinations of spectral index, flux and  $\gamma_{\min}$  considered. A closer inspection of Fig. 15 shows that for LHS1,

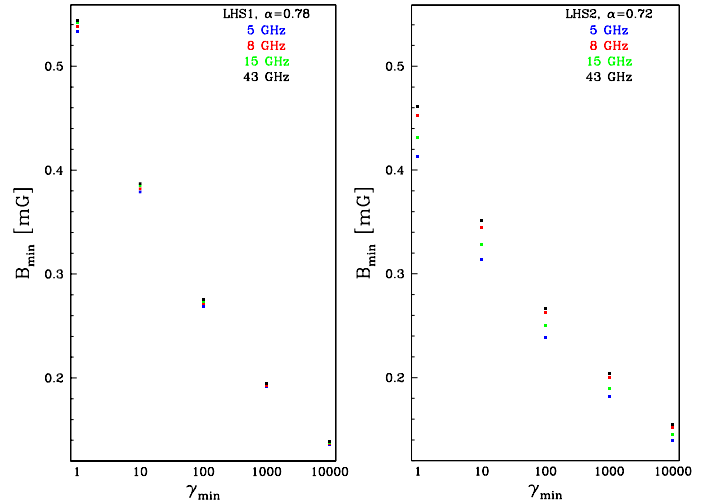


**Fig. 15.** Magnetic field strength, using the minimum energy assumption, calculated for 5, 8, 15, and 43 GHz versus the assumed minimum Lorentz factor for the electrons. *Left:* the secondary hotspot, LHS1. *Right:* the primary hotspot, LHS2.

there is good agreement between the  $B_{\min}$  values across the frequency range for a given  $\gamma_{\min}$ , with relative differences on the order of 2%. For LHS2 the scatter is somewhat larger, with relative differences on the order of 12% for a given  $\gamma_{\min}$ . For  $\gamma_{\min} \geq 100$  the minimum magnetic field strengths of LHS1 and LHS2 are broadly consistent with each other; the average  $\langle B_{\min, \text{LHS1}} \rangle$  and  $\langle B_{\min, \text{LHS2}} \rangle$  differ by about 7% for  $\gamma_{\min} = 100$  and  $\gamma_{\min} = 10000$ , while they are practically identical for  $\gamma_{\min} = 1000$ .

However, one should keep in mind the uncertainties that enter the calculation, particularly the adopted form of the source volume. For example, assuming a rectangular box, instead of a cylinder, for the volume, results in  $B_{\min}$  values that differ by about 7% from the values quoted in Table 5, i.e., comparable to the observed scatter. Thus, the minimum energy magnetic field values calculated with  $\alpha$  from the photometry fits are consistent with a single  $B_{\min}$  value for a given  $\gamma_{\min}$ .

## 5. Discussion

### 5.1. Magnetic field strength in the hotspots

In Table 5 we calculate the magnetic field strength assuming minimum energy conditions for a range of minimum Lorentz factors. We performed the calculation for the standard spectral index of 1, as well as for the best fit spectral index for both the original fluxes and the background corrected ones, for the 5, 8, 15 and 43 GHz observations. The largest uncertainty in that calculation is the volume of the hotspots, which we assumed to be cylinders. For the secondary hotspot (LHS1) we derived a magnetic field strength between 0.108 mG and 1.422 mG, with the largest difference due to the assumed minimum electron energy, i.e.,  $\gamma_{\min}$ , and secondary the assumed spectral index. The magnetic field strengths derived in the same manner for the primary hotspot (LHS2) are generally larger than those of LHS1 for  $\alpha = 1$  but smaller if we adopt  $\alpha$  from our photometry fits, ranging between 0.102 mG and 1.622 mG.

The question then is whether our  $B_{\min}$  calculations agree with what is theoretically expected. Considering that the primary hotspot is located where the jet first interacts with the ICM, while the secondary is either an aging and expanding hotspot or a splatter spot where the jet particles are redirected to, after losing some collimation and velocity, one would expect the magnetic field strength to be largest at the site of the shock in the primary hotspot. Instead Table 5 indicates very similar values for the hotspots. However, the very high degree of polarization observed in the ridge of the primary hotspot (Fig. 13) compared to the degree of polarization anywhere in the secondary hotspot, suggests that at least locally the magnetic field strength may be larger, but it is certainly more uniform.

Comparing Figs. 2, 3, and 5, we see that for the primary hotspot the bright ridge structure observed at 43 GHz fills only a small fraction of the area sampled by the aperture because the ridge is smaller than the resolution obtained below 43 GHz. If we identify the bright ridge with the actual shockfront, this means that for the primary hotspot we mostly sample the plasma as it is leaving the shockfront. This is in contrast to the secondary hotspot, where the bright linear features, likely associated with the shockfronts, are well resolved even at 5 GHz and fill about half the sampled area. This influences the measured flux density and, by extension, also the fitted spectral index, leading to lower  $B_{\min}$  values for LHS2. In other words, the magnetic field strength we calculate in the secondary hotspot is reasonably close to the magnetic field strength in the shockfront of that hotspot, but this is not the case for the primary hotspot. The lower magnetic field strength measured for the primary hotspot might be an indication that the magnetic field strength decreases on rather small scales, with the shockfront having a substantially higher magnetic field strength.

To test whether indeed the bright ridge of the primary hotspot has a larger magnetic field strength, we recalculated the minimum energy magnetic field strength, but for the flux in a much smaller area, using an aperture that enclosed just the ridge itself. We assumed that the slope index is the same as determined from Fig. 11. The derived magnetic field strength ranges from 0.26 mG to 0.80 mG, making it 1.5 times larger than the values quoted in Table 5 for either of the hotspots, confirming our above assumptions about the location of the shockfront. The minimum magnetic field strengths for the different assumed values of  $\gamma_{\min}$  are given in Table 6.

Carilli et al. (1991) derive magnetic field strengths between 0.25 and 0.35 mG from the 15 GHz image, using the minimum-energy calculation for a derived minimum Lorentz factor of 420

**Table 6.** Minimum energy magnetic field as a function of  $\gamma_{\min}$  determined from the bright ridge observed at 43 GHz in the primary (LHS2) hotspot in the western lobe of Cygnus A.

$\gamma_{\min}$	LHS2
	$B_{\min}$ [mG]
1	0.80
10	0.61
100	0.46
1000	0.35
10 000	0.27

**Notes.** We assume a spectral slope of 0.72, as determined for the larger area fitted using multifrequency data.

**Table 7.** Calculated values of the total energy in the hotspots of Cygnus A.

$\gamma$	Total energy [ $10^{50}$ J]			
	5 GHz	8 GHz	15 GHz	43 GHz
LHS1				
$10^0$	2.53	2.34	2.62	2.19
$10^1$	1.28	1.18	1.32	1.11
$10^2$	0.65	0.60	0.67	0.56
$10^3$	0.33	0.30	0.34	0.28
$10^4$	0.17	0.15	0.17	0.14
LHS2				
$10^0$	0.27	0.26	0.30	0.23
$10^1$	0.16	0.15	0.17	0.13
$10^2$	0.09	0.09	0.10	0.08
$10^3$	0.05	0.05	0.06	0.04
$10^4$	0.03	0.03	0.03	0.03

**Notes.** We used Eq. (5) assuming the minimum energy magnetic field values  $B_{\min}$  as given in Table 5, for background subtracted fluxes (cflux) and  $\alpha$  as calculated from fitting our photometry. In all cases, we have performed the calculation for five different  $\gamma$  values.

and assuming a spectral index of  $-0.5$  and a disk-like geometry for the hotspots. Stawarz et al. (2007) studied the hotspots in Cygnus A, adding *Spitzer* fluxes to constrain the emission mechanism and magnetic field strengths for the brighter hotspot in the lobe and counterlobe. For hotspot A, which we labeled LHS1, they derive a magnetic field strength of  $\sim 170 \mu\text{G}$  from comparing the radio and X-ray emission from the hotspot. This value is at the lower end of our derived magnetic field strengths. Stawarz et al. (2007) determine that the minimum Lorentz factor has to be smaller than 300, which is smaller than the value quoted by Carilli et al. (1991), and the values we derive in Sect. 5.3. However, Stawarz et al. (2007) use two rather different spectral indices of 0.28 and 1.2, and state that the energy density of the electrons is 6–8 times larger than in the magnetic field. Both the values by Carilli et al. (1991) and Stawarz et al. (2007) are consistent with the range in magnetic field values given in Table 5.

As a final step, we calculated the total energy present in the hotspots, using Eq. (5) and the  $B_{\min}$  values reported in Table 5. The total energy values are shown in Table 7.

There is good agreement between the total energy values for a given hotspot and a given  $\gamma$  across the radiobands. These values are consistent with expectations for a powerful radio galaxy, such as Cygnus A, where the energy stored in the lobes is on the order of  $10^{50}$ – $10^{52}$  J, and that of the hotspots is expected to be  $\sim 1\%$  of the total (e.g., Blundell et al. 1999; Stawarz et al. 2007).

## 5.2. Spectral shape of the hotspots

The theoretical spectral index for first order Fermi relativistic shock ranges between 0.35 and 0.63. For both hotspots, for the background corrected higher frequency fluxes, we find larger values, 0.72 and 0.78 for the primary and secondary hotspot, respectively. However, these values are consistent with previous observations; Carilli et al. (1991) found a spectral index of 0.5 for medium frequencies and 1.0 for higher frequencies for the hotspots in Cygnus A. They also derive a spectral index of 0.7 for the lobes.

From Figs. 10 and 11 we determine that the spectrum of the primary hotspot flattens between 330 MHz and 1.4 GHz, while the spectrum of the secondary hotspot flattens between 1.4 and 5 GHz. The flattening is due to a curved electron energy spectrum and a varying magnetic field (Rudnick et al. 1994; Fig. 4 in Blundell & Rawlings 2000). At higher frequencies the fluxes of both hotspots are well fitted with a power-law model and we do not need a high frequency spectral break.

Several authors have determined the spectral shape of the hotspot spectra, with results that are dependent on the lowest and highest frequency data used, the resolution of the data used, as well as the definition of what constitutes the hotspot. Carilli et al. (1991) determined the spectral curvature of the hotspots using 4'5 resolution images, and as a result only study the secondary hotspot. At this resolution the secondary and primary hotspots are not completely separated, but the secondary hotspot will dominate the results. Carilli et al. (1991) find a lower frequency break at  $\sim 300$  MHz.

Carilli et al. (1991) also determine a high frequency break at 10 GHz, using data up to 375 GHz. From their Fig. 4, we see that there is very little curvature between 1.4 and 43 GHz, and that the break is determined from higher frequency observations. So the fact that we do not find a spectral break up to 43 GHz is likely due to the limited frequency range we use. From the high frequency spectral shape, Carilli et al. (1991) rejected the possibility that the flattening of the spectrum is caused by synchrotron self absorption (SSA) or by thermal absorption. For the former, the magnetic field strength needs to be on the order of one Gauss, much larger than the value for either equipartition or minimum energy. For the latter, the required electron density in the putative absorber is too large (Carilli et al. 1991).

## 5.3. Minimum electron Lorentz factor for the hotspots

From the calculated magnetic field strengths as a function of minimum electron energy, we calculated the minimum frequency using Eq. (3) of Blundell et al. (1999). As input we used the background corrected flux values for the 8 GHz image, using the measured spectral index. In all the following calculations we will use these data, unless otherwise indicated. The results are listed in Table 8 and plotted in Fig. 16. The results are more strongly dependent on the magnetic field value than the minimum Lorentz factor, and thus the largest uncertainty in the calculation are the assumption of minimum energy and the assumed volume for the hotspot.

Using the above assumptions, coupled with break frequencies between 1.4 and 5 GHz for the primary hotspot and between 330 MHz and 1.4 GHz for the secondary hotspot, we derive a range in  $\gamma_{\min}$  between 1640 and 3350 for the primary hotspot, and between 770 and 1660 for the secondary hotspot.

Several authors have determined  $\gamma_{\min}$  for the hotspots in Cygnus A and other radio galaxies. Generally, a value of a few hundred to a few thousand is derived, consistent with the range

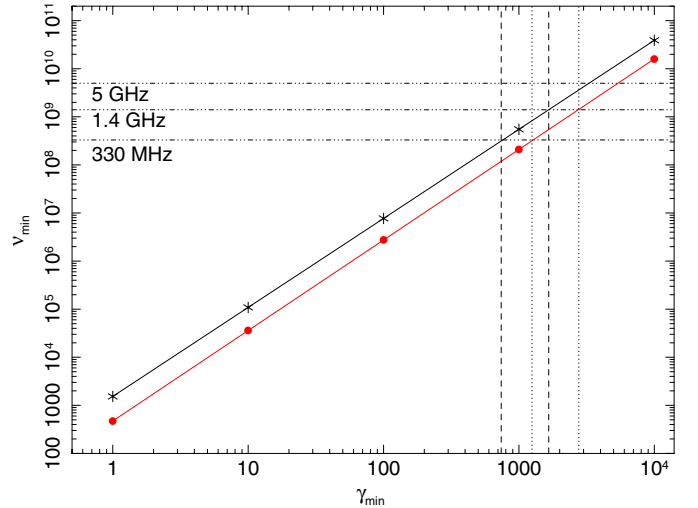


**Fig. 16.** Minimum frequency as a function of  $\gamma_{\min}$  for the primary hotspot (red filled circles) and secondary hotspot (asterisks) in the western lobe. We used the data as given in Table 8. The dash-dot-dot horizontal lines indicate the lower and upper limit to the break frequency for the secondary and primary hotspot. The dotted vertical lines indicate the range of allowed  $\gamma_{\min}$  for the primary hotspot. The dashed vertical lines indicate the same for the secondary hotspot.

**Table 8.** Minimum frequency,  $\nu_{\min}$ , as a function of  $\gamma_{\min}$  for the secondary (LHS1) and primary (LHS2) hotspots in the western lobe of Cygnus A.

$\gamma_{\min}$	LHS1 $\nu_{\min}$ (MHz)	LHS2 $\nu_{\min}$ (MHz)
1	$1.51 \times 10^{-3}$	$1.27 \times 10^{-3}$
10	0.11	0.10
100	7.61	7.36
1000	540.3	559.8
10000	$38.35 \times 10^3$	$42.55 \times 10^3$

**Notes.** We used the magnetic field strengths from the 8 GHz background corrected fluxes using the best fitting spectral slope as given in Table 5.

we determine for both hotspots. In the same manner, but with a different value for the magnetic field strength and a lower frequency break, Carilli et al. (1991) derived that the minimum electron Lorentz factor for the secondary hotspot in Cygnus A is  $420 \pm 20$ . This value is below our range, but only by a factor of  $\sim 2$ . The difference between our values and those of Carilli et al. (1991) can be explained by the fact that Carilli et al. (1991) use a different slope and images with 4'5 resolution, resulting likely in a larger assumed volume for the hotspot and contaminated fluxes.

Lazio et al. (2006) added the highest resolution 74 MHz data available to the data presented by Carilli et al. (1991), and found that the spectrum only flattens below 151 MHz, assuming that the hotspot flux in the 74 MHz data was diluted by a factor of 4. Using the low frequency fluxes, they found that a lower energy cut-off model gives a rather poor fit to the data points, but still favored this explanation over SSA and thermal absorption. A low energy cut-off was already proposed by Bell (1978a,b), reasoning that for an electron to be accelerated in a non-collisional shock, the gyroradius of the electron must be larger than the width of the shock. For the western hotspots combined, the best fit electron Lorentz factor was determined by Lazio et al. (2006) to be  $320 \pm 20$  for a fitted (resolution-dependent) lower break frequency of  $110 \pm 20$  MHz.

It is clear that the spectral shape of the hotspot spectra in Cygnus A will only be correctly determined if high-resolution images over a large range in frequency (74 MHz to at least 100 GHz) become available.

Perlman et al. (2010) derived a minimum Lorentz factor of  $\sim 1840$  for the southern hotspot of 3C 445, the ratio of the mass of the proton to that of an electron. For the same hotspot, the authors derived a low magnetic field strength,  $21.5 \mu\text{G}$ . Godfrey et al. (2009) studied the radio and X-ray emission from the hotspots in PKS 1421–490. Fitting the radio and optical fluxes with a one-zone synchrotron self-Compton emission, they concluded that the minimum Lorentz factor is about 650, or higher if beaming is important. The authors derived a magnetic field strength of 3 mG, similar to the values we derive.

Steenbrugge et al. (2008) determined a  $\gamma_{\min} \lesssim 10^3$  from the X-ray and radio flux limits on the current and previous jet emission in Cygnus A. This result is consistent with the results presented here for the secondary hotspot. For the primary hotspot we find somewhat larger values for  $\gamma_{\min}$ . However, we likely underestimate the magnetic field strength for the shock in the primary hotspot, and any increase in the magnetic field strength will lower the range in  $\gamma_{\min}$ . Assuming an increase in magnetic field strength of 50% for the primary hotspot (see Sect. 5.1) by choosing a smaller aperture leads to a 20% decrease in  $\gamma_{\min}$ . Considering the assumptions, the agreement between these two independent methods for the minimum Lorentz factor of the electrons in the jet and hotspots of Cygnus A is very good.

A similar method to that used by Steenbrugge et al. (2008) was applied by Blundell et al. (2006) to the eastern hotspot and lobe of 6C0905+3955. Blundell et al. (2006) used the lack of X-ray emission from the eastern hotspot, the observed X-ray emission from the eastern lobe, and the fact that the minimum Lorentz factor of the electrons in the lobe should be about a tenth of that of the electrons in the hotspot because of adiabatic expansion. They determined a minimum Lorentz factor on the order of  $10^4$  for the eastern hotspot of 6C0905+3955. Considering the different assumptions and uncertainties, the result for 6C0905+3955 is largely consistent with the results derived for Cygnus A. Thus, a rather large minimum Lorentz factor might be a common feature in jets and hotspots of radio galaxies.

#### 5.4. Comparison with the lobe spectra

If there is no in situ particle acceleration ongoing in the lobes, then the synchrotron-emitting electrons were last accelerated in the hotspots, and the energy distribution of the electrons should be the original energy distribution convolved with the loss mechanisms present. The dominant loss mechanism for electrons in the lobes is adiabatic expansion, either from the over-pressurized hotspots into the lobes, or from the over-pressurized lobes into the ICM. Rudnick et al. (1994) confirmed this for Cygnus A by showing that the emission from different parts of the lobe and the hotspots have the same spectral shape, consistent with the energy-independent losses caused by adiabatic expansion (Scheuer & Williams 1968). Synchrotron and inverse-Compton losses mostly affect the high energy electrons present in the hotspots or just outside the hotspots. The observed spectral shape depends on the electron energy distribution and the magnetic field strength present at the location of the emitting electron. If we make the simplifying assumption that the magnetic field is homogeneous on scales of the lobe (e.g., Scheuer & Williams 1968; Rudnick et al. 1994), then we can ignore the effect of the magnetic field on the spectral shape of both lobes.

Scheuer & Williams (1968) and Blundell et al. (1999) showed that if there is a minimum Lorentz factor for the electrons in the hotspots, then this Lorentz factor decreases by a factor of  $\sim 10$  in the full lobe spectra, because of the adiabatic expansion the electrons undergo, for assumed pressure ratios between the hotspot and the lobe. Assuming that the magnetic field only changes because of adiabatic expansion between the hotspots and the lobe, one can compare the minimum Lorentz factor for the electrons obtained from fitting the hotspot spectra with  $\sim 10$  times the minimum Lorentz factor for the electrons in the lobes. Alternatively, the low-frequency break should be a factor of 100 higher in the hotspots compared to the lobe,  $\nu_{\text{spot}} = 100 \nu_{\text{lobe}}$ .

The low-frequency break as obtained in Figs. 10 and 11 is between 330 MHz and 1.4 GHz for LHS1, and between 1.4 and 5 GHz for LHS2. From Fig. 1a in Rudnick et al. (1994) we see that the integrated lobe spectrum peaks at about 50 MHz. Duffy & Blundell (2012) found a peak frequency of approximately 23 MHz, refitting the integrated spectrum.

The observed range in low-frequency break in the secondary hotspot, LHS1, is smaller than what we would expect from the low-frequency peak observed in the lobes. However, the low-frequency break of LHS2, the primary hotspot, is consistent with the frequency at which lobe emission peaks. The above results are consistent with the lobe spectra being dominated by electrons accelerated in LHS2.

Duffy & Blundell (2012) fitting a curved electron distribution for the electrons in the lobes, and using the observationally determined  $\gamma_{\min}$  of a few  $10^3$ , calculated a magnetic field strength *in the lobes* of  $\sim 3.5 \times 10^{-3}$  nT (35 nG), which is about two orders of magnitude below the expected equipartition or minimum energy magnetic field *for the hotspots*.

#### 5.5. Spectral ages of the hotspots

Using a frequency value for the high-frequency break in the hotspot spectrum, Carilli et al. (1991) derive a synchrotron age of 0.12 Myr for the secondary hotspot in the lobe. We do not detect a high-frequency break, likely because of the limited frequency range we use at higher frequencies, and the low-frequency break, and perhaps also because of the higher resolution of the data used.

In the following calculation we make the assumption that adiabatic expansion and the change in magnetic field strength within the hotspots, as defined by us, can be neglected, in contrast to the situation for lobe spectra (Blundell & Rawlings 2001). We will also assume that the lower break frequency measured in the hotspots is determined by synchrotron processes, and not the minimum Lorentz factor. To calculate the so-called spectral age, we combined our Eq. (6) (using background corrected fluxes and the best-fitting  $\alpha$  as determined for the 8 GHz data) with Eq. (3) of Blundell et al. (1999). We used the observationally determined range for the low-frequency break, shown in Fig. 16. This allowed us to calculate a specific  $\gamma_{\min}$  value, which was subsequently used to derive the corresponding  $B_{\min}$  through Eq. (3) of Blundell et al. (1999). Finally, we used Eq. (1) of Carilli et al. (1991) to calculate the age, assuming for the high-frequency break either 12 GHz as derived by Carilli et al. (1991) or 43 GHz.

For LHS1, taking the high-frequency break to be at 12 GHz as derived by Carilli et al. (1991) we find a synchrotron age of 0.16 Myr or 0.19 Myr, for a low-frequency break of 330 MHz or 1.4 GHz, respectively. This value is larger, but similar to the age derived by Carilli et al. (1991). Taking a high-frequency break

of 43 GHz, we find a range in synchrotron age between 0.086 and 0.1 Myr, which thus halves the age for the hotspot.

Repeating the calculation for LHS2, the primary hotspot, we use the same assumptions we find similar, but slightly larger synchrotron ages, namely from 0.18 to 0.20 Myr and from 0.094 to 0.106 Myr, depending on the choice of low- and high-frequency breaks. A older synchrotron age seems unrealistic and is a result of particle acceleration in LHS2 occurring in a region much smaller than we originally fitted. Taking the flux measured in the small aperture around the bright ridge in the 43 GHz and assuming low-frequency breaks of 1.4 and 5 GHz and a high-frequency break of 43 GHz, we find, as expected, younger synchrotron ages ranging between 0.039 Myr and 0.044 Myr.

The precession period for the best fit jet speed is 0.24 Myr (Steenbrugge et al. 2008). Thus the estimated synchrotron age derived for the secondary hotspot, assuming a high-frequency break at 12 GHz, is somewhat younger but of the same order of magnitude as the jet precession period. The hotspot advance speed is somewhat uncertain, but for Cygnus A values of  $0.02c$  and  $0.005c$  are often used (Muxlow et al. 1988; Alexander & Pooley 1996). Assuming a constant hotspot advance speed, these values result in an age of the current jet activity in Cygnus A between 2 and  $8 \times 10^7$  years. Comparing this to the estimated synchrotron ages of the hotspots derived above, we see that the source lifetime is 105 to 500 times larger than the age of the secondary hotspot. We thus conclude that any given hotspot is only observable for a very short part of the lifetime of Cygnus A, and possibly, a large fraction of this time it is not even strongly accelerating electrons.

We can also estimate a dynamical age for the hotspots, assuming the plasma velocities derived by Carilli et al. (1991) and given in the next subsection. Using the 8 GHz data to determine the size of the hotspot, and taking an outflow velocity of  $0.07c$  for both hotspots, we find that an electron escapes the secondary hotspot in 50 000 years, and the primary hotspot in 30 000 years. The dynamical age is about a third of the estimated synchrotron age for the primary hotspot assuming the magnetic field as derived for the ridge at 43 GHz. The synchrotron age of the secondary hotspot is much larger than the dynamical escape time, indicating that either a fraction of the electrons have a much smaller velocity, or that scattering is important. The dynamical age for the secondary hotspot is consistent with the minimum time (50 000 years) since last particle acceleration took place, as derived by Wright & Birkinshaw (2004) from the detection of 230 GHz emission from the secondary hotspot.

As the primary hotspot is at least 30 000 years old (dynamical timescale) and most likely at least 70 000 years old, it is possible that sometime between 50 000 and 70 000 years ago, when the primary hotspot was created, the secondary hotspot stopped actively accelerating electrons. If the weak radio and X-ray emission feature identified in Fig. 9 is indeed a very young hotspot, this would indicate that in Cygnus A a new hotspot is formed about every 50 000 years, possibly linked to jet precession.

### 5.6. Plasma velocities and the current state of LHS1

Carilli et al. (1991) derive an outflow velocity of  $0.07c$  for LHS1 from its synchrotron age. We note that they did not study the primary hotspot, but we will assume the same outflow velocity for it. Assuming that the shock is a nonradiative shock, then the inflow velocity to the shock is 4 times larger or  $\sim 0.28c$ . This is similar, although somewhat smaller, than the best fit jet speed of  $0.35c$  determined from precession

by Steenbrugge & Blundell (2008). It thus seems that a strong shock occurs in LHS2, the primary hotspot, and that the inflow and outflow velocities for LHS1 are rather similar. If we assume that the shocked plasma does flow towards the secondary hotspot, and neglect de-acceleration of the electrons along the way, an inflow velocity between  $0.07c$  (assuming  $0.28c$  as the jet speed) and  $0.0875c$  (assuming the best fit jet speed of  $0.35c$ ) is calculated. This would lead, in the case of a strong shock, to an outflow velocity of  $0.0175c$  or  $0.022c$ , respectively, for the assumptions above. Even for the maximum jet speed allowed from modeling the precession,  $0.5c$  (Steenbrugge et al. 2008), the outflow velocity of LHS1 is  $0.031c$ , less than half the value determined by Carilli et al. (1991). Therefore, the shock in LHS1 is a weak shock, if a shock at all. This indicates that the secondary hotspot in the eastern lobe of Cygnus A is not a splatter spot, but rather an aging hotspot potentially with plasma still entering that is undergoing a weak shock at most.

This conclusion is consistent with the much smaller size of the likely shockfront observed in LHS2, the primary hotspot, the much higher level of polarization at 43 GHz for that hotspot, and the fact that the linear feature, likely the shockfront, observed in total emission in LHS1 disappears in polarized light.

### 5.7. Shift in peak luminosity with frequency

Although a shift in centroid and peak emission for the hotspots between low and high frequencies has not been discussed in the literature, shifts between the radio and X-ray emission have been observed rather frequently (e.g., Erlund et al. 2010). The explanation for the shift between radio and X-ray emission given for different sources and by different authors is quite varied. There is no agreement on the physical process producing the X-ray emission, which could be inverse-Compton scattering of either the cosmic microwave background photons (Blundell et al. 2006), inverse-Compton scattering of the low frequency synchrotron photons or synchrotron emission in models with two different electron distributions and a quickly changing magnetic field strength. Likely, the process is different for different hotspots and depends on the history of the source.

Interestingly, in the case of Cygnus A, there is no significant shift between the radio and X-ray emission for the secondary hotspot, while there is for the primary hotspot; moreover the radio and X-ray emission from the jet knot or youngest hotspot (Fig. 9) are even separated. This suggests that the shift may be related to the age of the hotspot. Furthermore, in the case where only the electron energy distribution is different, one would expect to see radio emission over the entire X-ray emitting area, because of the rapid synchrotron cooling of X-ray synchrotron emitting electrons. Clearly this is not the case for the primary hotspot.

A potential picture explaining this is that the largest magnetic field strength and the shock occur where we observe the X-ray emission. Outside the shockfront the magnetic field decreases rapidly, lowering the frequency at which the electrons emit. A further lowering of the frequency of emission is due to the short synchrotron lifetimes of the electrons emitting in the X-ray band and adiabatic expansion between the shockfront and the rest of the hotspot. From the two different apertures fitted to the primary hotspot, we know that the minimum energy magnetic field strength derived varies over small scales. Hence, it seems reasonable that at least part of the shift in peak emission is explained by a difference in magnetic field strength, and the fact that the accelerated electrons leave the shockfront to fill the rest of the hotspot.

## 6. Conclusions

We have studied the high-resolution 151, 330 MHz and 5, 8, 15 and 43 GHz images of Cygnus A and performed a detailed analysis of the two radio-bright hotspots in the western lobe. In the 43 GHz images, we resolve for the first time a bright ridge in the primary hotspot, likely the site of the shock.

Comparing the centroid for both hotspots for the different frequencies, we detect a significant shift for both hotspots between the low frequencies and 5 GHz and above. This shift can be explained by a rapid decrease in the magnetic field strength between the shockfront and the rest of the hotspots. This rapid decrease in magnetic field strength was also derived from the fact that the standard aperture used to study the primary hotspot gives a lower magnetic field strength, than that of the secondary hotspot. However, repeating the calculation only for the bright rim in the 43 GHz image, the minimum energy magnetic field strength is found to be 1.5 times larger.

We derived minimum energy magnetic field strengths for both hotspots, which range between 0.14 to 0.54 mG for LHS1 and between 0.14 and 0.46 mG for LHS2. Repeating the magnetic field calculation for LHS2 in the 43 GHz data alone and using a small aperture that enclosed only the observed bright ridge, we found a minimum energy magnetic field strength ranging between 0.26 to 0.80 mG. These values allowed us to determine the minimum Lorentz factor for the electrons in the hotspots to be a few hundred to a few thousand. This value is consistent with the independent measurement by [Steenbrugge et al. \(2008\)](#) and for LHS2 with the fact that in the lobe the spectrum turns over between  $\sim 23$  and  $\sim 50$  MHz. The estimated synchrotron age of the secondary hotspot is much smaller than the age of the source, and is comparable to the precession period.

Finally, from the relatively low fractional polarization and the outflow velocity for LHS1 derived by [Carilli et al. \(1991\)](#), we conclude that the secondary hotspot, LHS1, is not a splatter spot, but is an aging hotspot which possibly still weakly shocks incoming plasma.

Further analysis of Cygnus A will undoubtedly benefit from higher-resolution images over a large range in frequency, 74 MHz up to at least 100 GHz.

*Acknowledgements.* We thank the anonymous referee for a constructive report. S.P. and K.C.S. gratefully acknowledge the support from ALMA-CONICYT grant 31110019.

## References

- Alexander, P., & Pooley, G. G. 1996, in *Cygnus A – Study of a Radio Galaxy*, Proc. Greenbank Workshop (CUP), 149
- Bell, A. R. 1978a, *MNRAS*, 182, 147
- Bell, A. R. 1978b, *MNRAS*, 182, 443
- Blundell, K. M., & Fabian, A. C. 2011, *MNRAS*, 412, 705
- Blundell, K. M., & Rawlings, S. 2000, *AJ*, 119, 1111
- Blundell, K. M., & Rawlings, S. 2001, in *Particles and Fields in Radio Galaxies Conference*, eds. R. A. Laing, & K. M. Blundell, ASP Conf. Ser., 250, 363
- Blundell, K. M., Rawlings, S., & Willott, C. J. 1999, *AJ*, 117, 677
- Blundell, K. M., Fabian, A. C., Crawford, C. S., Erlund, M. C., & Celotti, A. 2006, *ApJ*, 644, L13
- Carilli, C. L., & Barthel, P. D. 1996, *A&AR*, 7, 1
- Carilli, C. L., Perley, R. A., Dreher, J. W., & Leahy, J. P. 1991, *ApJ*, 383, 554
- Carilli, C., Perley, R., Bartel, N., & Dreher, J. 1996, *The jets in Cygnus A: from pc- to kpc-scales*, eds. C. L. Carilli, & D. E. Harris, 76
- Carilli, C. L., Kurk, J. D., van der Werf, P. P., Perley, R. A., & Miley, G. K. 1999, *MNRAS*, 311, 2581
- Cox, C. I., Gull, S. F., & Scheuer, P. A. G. 1991, *MNRAS*, 252, 558
- Duffy, P., & Blundell, K. M. 2012, *MNRAS*, 421, 108
- Erlund, M. C., Fabian, A. C., Blundell, K. M., Crawford, C. S., & Hirst, P. 2010, *MNRAS*, 404, 629
- Godfrey, L. E. H., Bicknell, G. V., Lovell, J. E. J., et al. 2009, *ApJ*, 695, 707
- Lazio, T. J. W., Cohen, A. S., Kassim, N. E., et al. 2006, *ApJ*, 642, L33
- Leahy, J. P., Muxlow, T. W. B., & Stephens, P. W. 1989, *MNRAS*, 239, 401
- Ledlow, M. J., Owen, F. N., & Miller, N. A. 2005, *AJ*, 130, 47
- Longair, M. S. 1994, *High energy astrophysics*, Vol. 2, Stars, the Galaxy and the interstellar medium (Cambridge University Press)
- Muxlow, T. W. B., Pelletier, G., & Roland, J. 1988, *A&A*, 206, 237
- Owen, F. N., Ledlow, M. J., Morrison, G. E., & Hill, J. M. 1997, *ApJ*, 488, L15
- Perley, R. A., & Carilli, C. L. 1996, *The structure and polarization of Cygnus A at  $\lambda$  3.6 cm*, eds. C. L. Carilli, & D. E. Harris, 168
- Perlman, E. S., Georganopoulos, M., May, E. M., & Kazanas, D. 2010, *ApJ*, 708, 1
- Rudnick, L., Katz-Stone, D. M., & Anderson, M. C. 1994, *ApJS*, 90, 955
- Scheuer, P. A. G. 1982, in *Extragalactic Radio Sources*, eds. D. S. Heeschen, & C. M. Wade, IAU Symp., 97, 163
- Scheuer, P. A. G., & Williams, P. J. S. 1968, *ARA&A*, 6, 321
- Stawarz, Ł., Cheung, C. C., Harris, D. E., & Ostrowski, M. 2007, *ApJ*, 662, 213
- Steenbrugge, K. C., & Blundell, K. M. 2008, *MNRAS*, 388, 1457
- Steenbrugge, K. C., Blundell, K. M., & Duffy, P. 2008, *MNRAS*, 388, 1465
- Steenbrugge, K. C., Heywood, I., & Blundell, K. M. 2010, *MNRAS*, 401, 67
- Steenbrugge, K. C., Blundell, K. M., & Pyrzas, S. 2014, *A&A*, 563, A131
- Williams, A. G., & Gull, S. F. 1985, *Nature*, 313, 34
- Wright, M. C. H., & Birkinshaw, M. 2004, *ApJ*, 614, 115